METHODS

Near-Field Diffuse Scattering Measurement Technique for Use With Effective Roughness Model

JUNSEOP LEE[1], (Student Member, IEEE), AND KANGWOOK KIM[2], (Senior Member, IEEE)

[1]School of Mechanical Engineering, Gwangju Institute of Science and Technology, Gwangju 61005, South Korea
[2]School of Electrical Engineering and Computer Science, Gwangju Institute of Science and Technology, Gwangju 61005, South Korea

Corresponding author: Kangwook Kim (mkkim@gist.ac.kr)

ABSTRACT A compact method for extracting the parameters of the effective roughness model is introduced, which predicts statistical field scattering from rough surfaces. The proposed method includes quasi-plane wave generation using a parabolic reflector, sampling the near-field data, transforming the near-field data to the far field, and fitting using a cost function that provides for a greater contribution from the diffuse scattering than conventional methods. The proposed method was validated through a set of experiments using two materials under test with distinct roughness characteristics at 40 GHz. The scattering patterns were measured, and the directive model parameters were extracted using conventional and proposed methods. The results were compared to show that the proposed method is consistent with the conventional results, confirming its validity. The proposed method combines the advantages of a compact range and near-field measurements and can be used as an effective technique for extracting site-specific model parameters within indoor environments across mm-wave bands.

INDEX TERMS Directive model, effective roughness model, millimeter wave measurements, near-field to far-field transformation technique, parameter extraction, reflector antennas, surface roughness.

I. INTRODUCTION

The rapid expansion of wireless applications in both indoor and outdoor urban environments has led to an increased demand for electromagnetic wave propagation models that account for the influences of building structures and materials [1], [2], [3]. Fresnel's equation describes the reflection of electromagnetic waves at the boundary between two media with waves reflected in the specular direction. This equation is also applicable to building surfaces assuming that they are smooth and uniform. However, when surfaces are rough, electromagnetic waves diffuse or scatter in multiple directions. This phenomenon is particularly noticeable when the surface roughness is comparable to the wavelength. Several

The associate editor coordinating the review of this manuscript and approving it for publication was Kai Lu.

case studies have reported that the effect of material surfaces reduces the prediction accuracy of propagation in applications such as 5G NR and automotive radar using mm-wave bands [4], [5], [6]. To enhance the prediction accuracy of emerging high-frequency band applications, it is essential to incorporate diffuse-scattering models into existing models [7], [8].

Various diffuse-scattering models have been developed using both analytical and numerical methods [9], [10], [11], [12], [13], [14]. Analytical methods such as the small perturbation method and Kirchhoff approximation require boundary conditions and statistical information on the geometry. Consequently, detailed geometric measurements are required for the application of these methods. However, for actual buildings, obtaining detailed measurements may be challenging because of the scale of structures. In contrast, numerical

methods use a realistic mesh structure to obtain a diffuse pattern, replacing the need for analytical boundary conditions. However, these methods also require detailed geometry and dielectric constant measurements.

As an alternative approach, the effective roughness (ER) model was proposed to predict the statistical field scattered from rough surfaces based on empirical measurements [15]. The ER model assumes that the material under test (MUT) with an actual rough surface has a flat surface geometry that produces a coherent specular reflection and incoherent diffuse scattering under plane-wave illumination. When applied to building- or city-level propagation, the coherent component predicts polarization and phase information from ray optics perspective, whereas the incoherent component predicts statistical diffuse scattering that disregards polarization and phase information. Although not as rigorous a solution as the analytical method, the ER model has been shown to produce predictions similar to the actual measurement results from MUTs with random roughness when it is integrated with conventional interactions [16].

ER models, such as the Lambertian, directive, double-lobe, and hybrid models, exhibit distinct patterns [17], [18], [19]. An appropriate pattern should be determined empirically based on the specific application requirements. Once a model is selected, its parameters are determined by fitting them to the measured values. ER models are practical because they can be applied without requiring information on the dielectric constant or a statistical definition of surface roughness.

Diffuse pattern measurements are typically produced by placing a transmitting antenna in the far-field to illuminate an MUT with a plane wave. Ideally, the diffuse scattering pattern should be measured using an antenna in the far field of the illuminated area of the MUT. However, for MUTs preinstalled in indoor environments, satisfying far-field conditions can be challenging due to its spatial limitation, particularly at higher frequencies [20]. To address this aspect, we propose a compact measurement method for model parameter extraction that can be applied even when an adequate far-field range is unavailable. In the proposed method, the MUT is illuminated by a quasi-plane wave generated by a parabolic reflector antenna, and a diffuse scattering pattern is obtained by transforming the near-field measured data. The proposed method was validated using actual measurements and comparisons with the conventional measurement approach.

II. DIRECTIVE MODEL AND MODEL PARAMETERS

In this study, we focus on the directive model, which has been effectively used in practical applications [21], [22], [23]. The scattering of electromagnetic waves from an MUT is shown in Fig. 1(a). A global coordinate system is set up centered on the MUT, with the MUT surface aligned in the x-y plane. In addition, a local coordinate system is defined with the center at the reflection point Q on the MUT. θ_i and θ_r are the incident and specular reflection angles, respectively. A transmitting antenna located at (r_i, θ_i, ϕ_i) radiates the total power of P_t with a gain of G towards the center of the
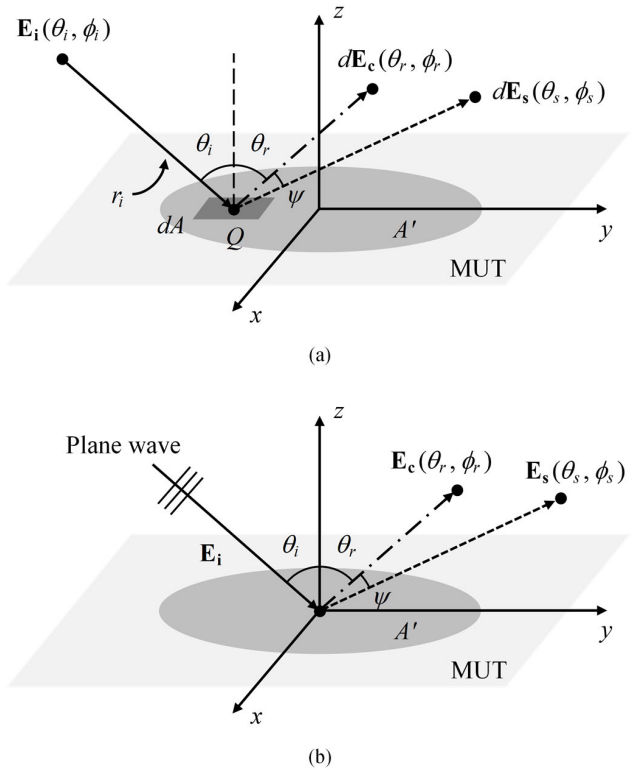

FIGURE 1. Scattering of electromagnetic waves: (a) point source illumination and (b) plane-wave illumination.

MUT, illuminating the footprint area A'. If the surface of the MUT is smooth and uniform, the scattered electromagnetic waves from the incident wave on each infinitesimal area dA can be represented solely by the coherent component $d\mathbf{E_c}$. If the surface of the MUT is rough, with a geometry that can be described using random characteristics, the incoherent component $d\mathbf{E_s}$ must also be included. At an observer point, the total reflected field from the footprint area A' is the superposition of $\mathbf{E_c}$ and $\mathbf{E_s}$, which are obtained by integrating $d\mathbf{E_c}$ coherently and $d\mathbf{E_s}$ incoherently, respectively.

In the directive model, the incoherent components can be described as [17]

$$\left| \mathbf{E_s^{model}} (\theta_s, \phi_s) \right|^2 = \int_{A'} \frac{\eta G_t P_t}{2\pi r_i^2} |\Gamma|^2 |S|^2$$
$$\cdot \left(\frac{1 + \cos \psi}{2} \right)^\alpha \frac{\cos \theta_i}{F_\alpha} dA \quad (1)$$

where $F_\alpha = \int_0^{2\pi} \int_0^{\pi/2} \left(\frac{1+\cos \psi}{2} \right)^\alpha \sin \theta_s d\theta_s d\phi_s$, ψ is the angle difference between the directions of the specular reflection (θ_r, ϕ_r) and the observation (θ_s, ϕ_s); η is intrinsic impedance of the medium; F_α is the surface integral value of the directive model scattering lobe pattern within the ranges of $0 < \theta_s < \pi/2$ and $0 < \phi_s < 2\pi$; α is the model directivity; and Γ, R, and S represent the reflection coefficient, reflection reduction factor, and scattering factor, respectively, which are

defined as

$$|\Gamma|^2 = \frac{P_r}{P_i}, \quad |R|^2 = \frac{P_c}{P_r}, \quad \text{and } |S|^2 = \frac{P_s}{P_r}, \qquad (2)$$

where P_i is the total power incident on the MUT, and P_r is the total power reflected from the MUT. The total reflected power can further be divided into a coherent power component P_c and incoherent power component P_s. Thus,

$$P_r = P_c + P_s \text{ and } |R|^2 + |S|^2 = 1. \qquad (3)$$

As illustrated in Fig. 1(b), when the transmitting and receiving antennas are located in the far field of the MUT, the incident electromagnetic wave can be locally assumed to be a plane wave, and θ_i may be considered constant over A'. Consequently, the incident field intensity and the total power radiated from the transmitting antenna can be expressed as

$$|\mathbf{E_i}|^2 = \frac{\eta G_t P_t}{2\pi r_i^2} = \frac{2\eta P_i}{A' \cos \theta_i}. \qquad (4)$$

Under these conditions, the incoherent component of the directive model can be rewritten as

$$\left| \mathbf{E_s^{model}}(\theta_s, \phi_s) \right|^2 = \frac{2\eta P_i}{F_\alpha} |\Gamma|^2 |S|^2 \left(\frac{1 + \cos \psi}{2} \right)^\alpha. \qquad (5)$$

The total reflected power from the MUT is obtained by integrating the reflected power in all directions. That is,

$$P_r = \frac{1}{2\eta} \int_0^{2\pi} \int_0^{\pi/2} \left| \mathbf{E_{r, MUT}}(\theta_s, \phi_s) \right|^2 \sin \theta_s d\theta_s d\phi_s, \qquad (6)$$

where $\mathbf{E_{r,MUT}}(\theta_s, \phi_s)$ is the field reflected from the MUT measured at observation angle (θ_s, ϕ_s). If a flat perfect electric conductor (PEC) is placed on the surface of the MUT, the total reflected power is equal to the total incident power since $|\Gamma_{PEC}| = 1$. Therefore, the total power incident on the MUT can be obtained as

$$P_i = \frac{1}{2\eta} \int_0^{2\pi} \int_0^{\pi/2} \left| \mathbf{E_{r, PEC}}(\theta_s, \phi_s) \right|^2 \sin \theta_s d\theta_s d\phi_s, \qquad (7)$$

where $\mathbf{E_{r,PEC}}(\theta_s, \phi_s)$ is the field reflected from the flat PEC measured at observation angle (θ_s, ϕ_s).

The reflection coefficient Γ can then be determined from (6) and (7) as

$$|\Gamma|^2 = \frac{P_r}{P_i} = \frac{\int_0^{2\pi} \int_0^{\pi/2} \left| \mathbf{E_{r, MUT}}(\theta_s, \phi_s) \right|^2 \sin \theta_s d\theta_s d\phi_s}{\int_0^{2\pi} \int_0^{\pi/2} \left| \mathbf{E_{r, PEC}}(\theta_s, \phi_s) \right|^2 \sin \theta_s d\theta_s d\phi_s}. \qquad (8)$$

Equation (5) can then be rewritten using (7) as

$$\left| \mathbf{E_{s, MUT}^{model}}(\theta_s, \phi_s) \right|^2 = \frac{|\Gamma|^2 |S|^2}{F_\alpha} \left(\frac{1 + \cos \psi}{2} \right)^\alpha$$
$$\cdot \int_0^{2\pi} \int_0^{\pi/2} \left| \mathbf{E_{r, PEC}}(\theta_s, \phi_s) \right|^2 \sin \theta_s d\theta_s d\phi_s. \qquad (9)$$

The parameters S and α are obtained through fitting from the total reflected field. The scattered fields in the model are assumed to have equal magnitudes for the two orthogonal linearly polarized components, and due to their incoherent nature, the phases are disregarded [17].

III. PROPOSED PARAMETER EXTRACTION METHOD

In the previous section, we discussed the directive model parameters of the MUT for a geometry in which the transmitting and receiving antennas are located in the far field. If the transmitting and receiving antennas are in an outdoor space, the far-field conditions can be easily satisfied. However, it may be difficult to satisfy far-field conditions in many indoor scenarios, necessitating near-field measurements. The geometry shown in Fig. 2 was considered for indoor scenarios.
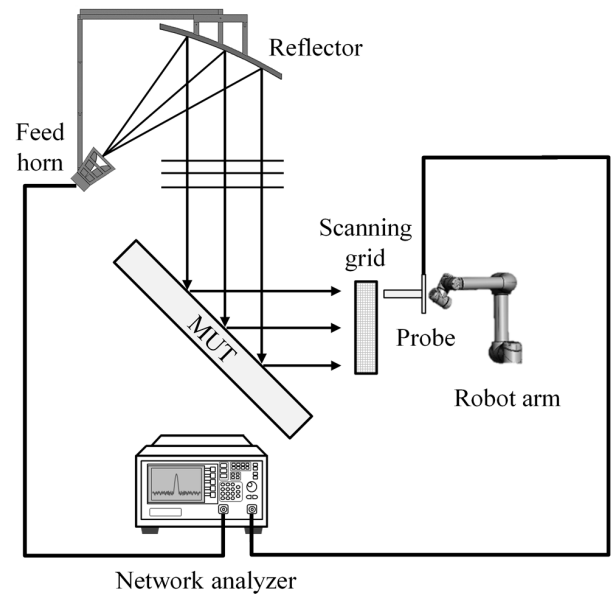

FIGURE 2. Top view of proposed near-field diffuse scattering measurement method.

Fig. 2 shows the top view of the setup of the proposed measurement method. Instead of positioning the transmitting antenna in the far field, a plane wave is generated in the near field using an offset parabolic reflector antenna. A virtual grid was established on a 2D plane perpendicular to the direction of specular reflection, and planar near-field (PNF) data were sampled at each grid point using a probe antenna. The field data obtained in the near field are then converted into far-field data using the near-field to far-field transformation (NTFT) technique. The parameters Γ, R, S, and α can be determined by fitting the transformed far field to the directive model.

A parabolic reflector with a feed-horn antenna at the focal point is used to generate a quasi-plane wave around the MUT. The reflector is designed such that the amplitude and phase variations in the equiphase plane around the MUT are small for the measurement accuracy [24]. An offset feed reflector
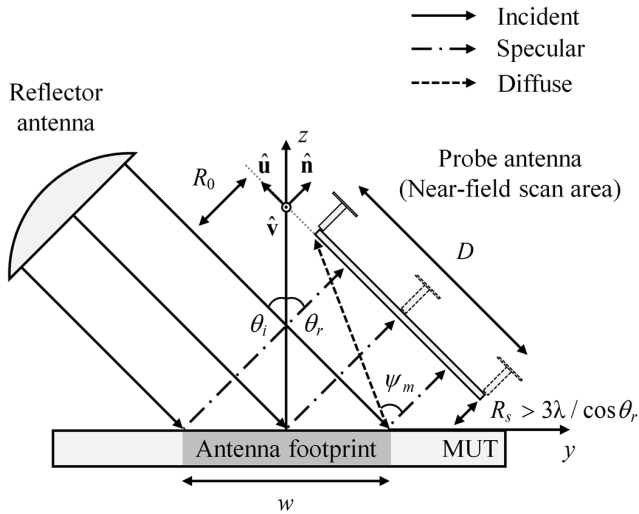
FIGURE 3. Planar near-field measurement dimensions.

is used to minimize the disturbances caused by the feed horn antenna.

Fig. 3 shows the dimensions of the near-field measurements for the proposed PNF scanning. Grid distance R_s is the shortest distance between the scanning grid points and the MUT along the $\hat{\mathbf{n}}$ direction, R_0 is the shortest distance measured from the scanning grid points to the antenna footprint, w is the major diameter of the antenna footprint on the MUT, ψ_m is the maximum observable angle of the diffuse scattering, D is the dimension of the scanning grid, and (u, v, n) are the axes of the local coordinates of the near-field grid. Note that R_s is not allowed to be larger than R_0 and needs to be in the range of $R_0 \geq R_s \geq 3\lambda / \cos\theta_r$ to suppress the multiple reflections between the MUT and the probe and also to suppress the exponentially decaying evanescent fields to approximately -150 dB in the lowest-order mode [25], [26], [27]. Moreover, for the scanning area covering the footprint reflected rays, $R_0 \tan\psi_m = w \cos\theta_r$. For $\psi_m \geq \psi_{m,\min}$, R_0 and R_s need to be selected such that $w \cos\theta_r / \tan\psi_{m,\min} \geq R_0 \geq R_s \geq 3\lambda / \cos\theta_r$. Then, the dimensions of the scanning grid can be established as $D = w \cos\theta_r + 2(R_0 - R_s)/ \tan\theta_r$ by assuming a square scanning grid whose center coincides with the specular ray from the center of the footprint area. The maximum observable angle of diffuse scattering can then be obtained as

$$\psi_m = \tan^{-1} \frac{w \cos\theta_r + (R_0 - R_s)/ \tan\theta_r}{R_0}. \tag{10}$$

The grid spacing, Δ_u and Δ_v should be smaller than $\lambda /(1 + \sin\psi_m)$ to minimize aliasing from diffuse scattering at the maximum observable angle [27], [28].

The flowchart in Fig. 4 shows the procedure for obtaining the directive model parameters Γ, R, S, and α using (8) and (9). To evaluate (8) and (9) in section II above, the measured field must be integrated across all directions. However, because most of the reflected power from the MUT
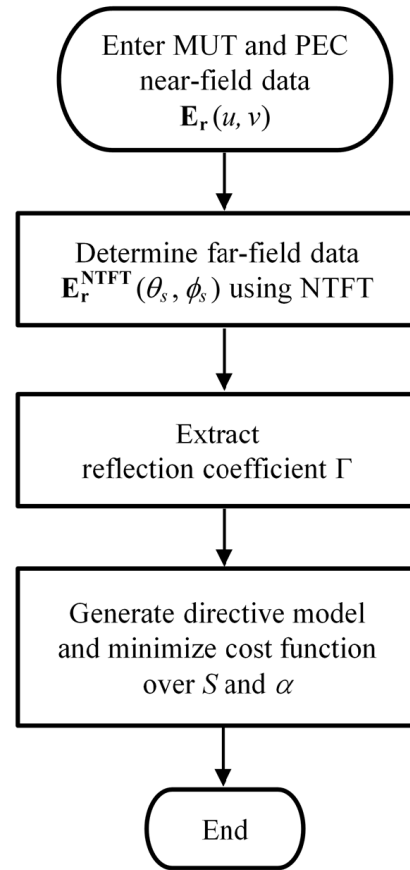

FIGURE 4. Fitting procedure flowchart.

is concentrated in the direction of the specular reflection, the total reflected power can be approximated to the total power passing through the near-field scanning area. Therefore, the far field obtained from the NTFT technique should be approximately the same as the results of (8) and (9).

The fitting algorithm starts with 2D near-field measurement data from the MUT and PEC using the method by means of plane-wave generation and near-field scanning. Upon completion of the NTFT, directive model generation and cost function evaluations are conducted to obtain the optimal fit parameters. Each step is performed in detail as follows.

Step 1. MUT and PEC near-field data acquisition from 2D planar scanning

In the proposed setup around the MUT, data are obtained on scanning grids to produce MUT-reflected near-field data. A PEC sheet is placed on top of the MUT, and the same measurement is repeated to produce PEC-reflected near-field data.

Step 2. MUT and PEC far-field data determination using NTFT

The NTFT technique is applied to the MUT- and PEC-reflected near-field data to obtain far-field data,

$$\mathbf{E_r^{NTFT}}(\theta_s, \phi_s) = \text{NTFT}\{\mathbf{E_r}(u, v)\}. \tag{11}$$

Step 3. Reflection coefficient extraction

The reflection coefficient is determined using (8), where the integration angle is limited to the maximum observable angle. Because most of the reflected power is concentrated in the specular direction, (8) can be applied by substituting the NTFT far-field data with limited integration angles.

$$
\begin{aligned}
|\Gamma|^2 &= \frac{P_r}{P_i} \\
&\simeq \frac{\int_{\phi_r-\psi_m}^{\phi_r+\psi_m} \int_{\theta_r-\psi_m}^{\theta_r+\psi_m} \left| \mathbf{E}_{\mathbf{r,MUT}}^{\mathbf{NTFT}}(\theta_s, \phi_s) \right|^2 \sin\theta_s d\theta_s d\phi_s}{\int_{\phi_r-\psi_m}^{\phi_r+\psi_m} \int_{\theta_r-\psi_m}^{\theta_r+\psi_m} \left| \mathbf{E}_{\mathbf{r,PEC}}^{\mathbf{NTFT}}(\theta_s, \phi_s) \right|^2 \sin\theta_s d\theta_s d\phi_s}.
\end{aligned}
$$
$$(12)$$

Step 4. Directive model generation and cost function evaluation for S and α

The directive model is generated using the Γ obtained from the previous step over the ranges of S and α. The reflection reduction factor R is also updated with S according to (3). The incoherent component with the ranges of limited integration angle is expressed as

$$
\begin{aligned}
&\left| \mathbf{E}_{\mathbf{s,MUT}}^{\mathbf{model}}(\theta_s, \phi_s) \right|^2 \\
&\simeq \frac{|\Gamma|^2 |S|^2}{F_\alpha} \left(\frac{1+\cos\psi}{2} \right)^\alpha \\
&\cdot \int_{\phi_r-\psi_m}^{\phi_r+\psi_m} \int_{\theta_r-\psi_m}^{\theta_r+\psi_m} \left| \mathbf{E}_{\mathbf{r,PEC}}^{\mathbf{NTFT}}(\theta_s, \phi_s) \right|^2 \sin\theta_s d\theta_s d\phi_s.
\end{aligned}
$$
$$(13)$$

The total reflected field is obtained by the summation of the coherent and incoherent components. The coherent component is represented by scaling NTFT far-field data of PEC.

$$
\left| \mathbf{E}_{\mathbf{r,MUT}}^{\mathbf{model}}(\theta_s, \phi_s) \right|^2 = \left| \mathbf{E}_{\mathbf{c,MUT}}^{\mathbf{model}}(\theta_s, \phi_s) \right|^2 + \left| \mathbf{E}_{\mathbf{s,MUT}}^{\mathbf{model}}(\theta_s, \phi_s) \right|^2
$$
$$(14)$$

where $\left| \mathbf{E}_{\mathbf{c,MUT}}^{\mathbf{model}}(\theta_s, \phi_s) \right|^2 = |\Gamma|^2 |R|^2 \left| \mathbf{E}_{\mathbf{c,PEC}}^{\mathbf{NTFT}}(\theta_s, \phi_s) \right|^2$.

The cost function is evaluated by comparing the total reflected field of the model with the measured field. The optimal model parameters S and α are determined when the cost function is minimized. The cost function may depend on the type of application.

Note that the small roughness assumption is used when we determine the reflection coefficient from (12). For surfaces with large roughness, the discrepancy between the actual reflected power and the reflected power collected by the scanning grid may be significant. This discrepancy can lead to an error in the determination of the reflection coefficient, which in turn could affect subsequent parameter fitting. Assuming that the incoherent components can be represented by a directive model, the error in the reflection coefficient can be

estimated using the following inequality:

$$
\begin{aligned}
&\frac{|\Gamma_{\text{total}}|^2 - |\Gamma_{\text{grid}}|^2}{|\Gamma_{\text{total}}|^2} \\
&= \frac{P_{r,\text{total}} - P_{r,\text{grid}}}{P_{r,\text{total}}} < \frac{P_{s,\text{total}} - P_{s,\text{grid}}}{P_{s,\text{total}}} \\
&= \frac{F_\alpha - \int_{\phi_r-\psi_m}^{\phi_r+\psi_m} \int_{\theta_r-\psi_m}^{\theta_r+\psi_m} \left(\frac{1+\cos\psi}{2} \right)^\alpha \sin\theta_s d\theta_s d\phi_s}{F_\alpha},
\end{aligned}
$$
$$(15)$$

where the subscripts 'total' and 'grid' denote the measurement from the upper half-space and grid space, respectively. The right-hand side error term of (15) is a function of both the model directivity α and the maximum observable angle ψ_m. The corresponding errors of 1, 5, and 10% are illustrated in Fig. 5. In the case of large roughness where α is small, a larger observable angle is required. For instance, $\psi_m > 50°$ is necessary to limit the error to 10% or less as $\alpha < 10$.
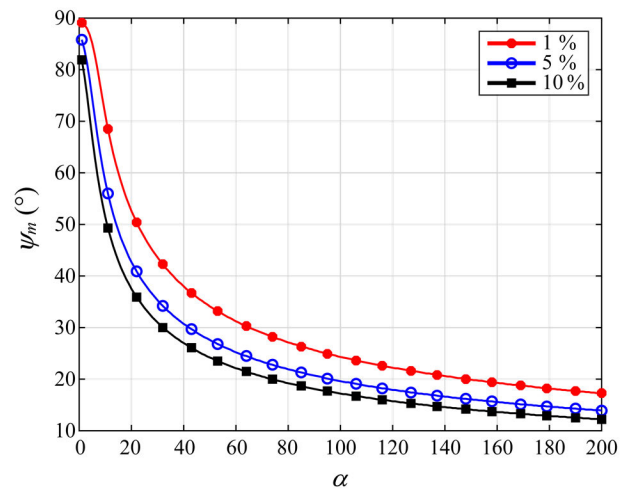

FIGURE 5. The maximum observable angle versus the model directivity for the tolerances of 1, 5, and 10% $|\Gamma|^2$ error.

The far-field measurements have the advantage of a wide maximum observable angle but are limited by the distance. With adequate setup dimensions, the near-field measurement can still extract far-field parameters, but with a more compact measurement setup. This compactness of the setup is a significant advantage compared to the far-field measurement. The further near-field measurement technique and associated error analysis methods are comprehensively described in [29].

IV. MEASUREMENT SETUP AND RESULT

An indoor experiment was conducted on rough materials to validate the effectiveness of the proposed fitting algorithm and measurement method. The MUTs with rough material surfaces were implemented on 150-mm-thick expanded polystyrene slabs. They were covered with water-soluble paint with a thickness of approximately 3.5 mm using either a plastering or a rolling method. To compare only the effects
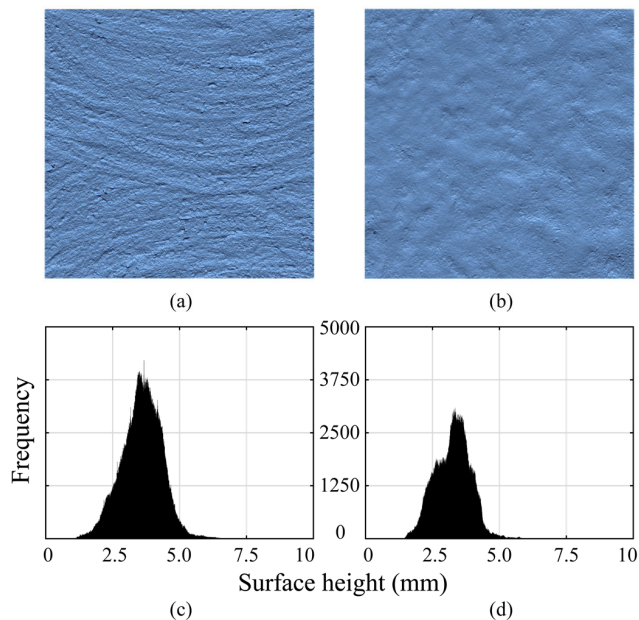
FIGURE 6. Photographs of rough surfaces made with (a) plastering and (b) rolling methods and (c), (d) corresponding height histograms measured with a 3D laser scanner.

TABLE 1. Statistical properties of implemented rough surface materials.

Implementation method	Statistical properties (µm)			RMS surface slope
	Standard deviation	Mean	Correlation length	
Plastering	758.98	3579.9	5160.9	207.98
Rolling	660.27	3259.3	9229.8	101.16

FIGURE 7. (a) E-plane ($\phi = 90°$) and (b) H-plane ($\theta = 90°$) far field patterns of the reflector antenna.

TABLE 2. Measurement setup parameter.

Parameter		Value
Tx antenna (Reflector)	F/D	1.4
	Gain	26.9 dBi
	XPD	36.5 dB
Probe antenna	Gain	7.0 dBi
	XPD	35.0 dB
Illumination	Target frequency	40 GHz
	Incident polarization	TE pol.
	Incident angle (θ_i)	45°
	Footprint major and minor diameters	164 mm × 90 mm
Near-field scanning dimension	Grid distance (R_s)	100 mm
	Grid spacing (Δ_u, Δ_v)	3.75 mm
	Numbers of grid points	51 × 51

of the rough surface without the influence of slab thickness, conductive paint was applied to the surface of the MUTs after the former paints had completely dried.

The surface height data were obtained using a 3D laser scanner to analyze the roughness of the MUTs, and their distributions are displayed as histograms in Fig. 6. Both plastering and rolling methods exhibit asymmetric Gaussian distributions or a linear combination of multiple Gaussian distributions. The surface roughness is expressed as the surface height standard deviation, correlation length, and root mean square (RMS) surface slope, and is tabulated in Table 1.

The reflector antenna was designed with a focal-length-to-diameter (F/D) ratio of 1.4 and an offset angle of 45° to enhance its cross-polarization performance. The reflector shape was fabricated using stereolithography 3D printing technology, and the surface was coated with a conductive paint. An A-INFO LB-45500 wideband ridged horn antenna was used as the feed, and the resulting co- and cross-polarization radiation patterns were measured using the near-field technique, as shown in Fig. 7. An A-INFO standard rectangular open-ended waveguide antenna with a gain of
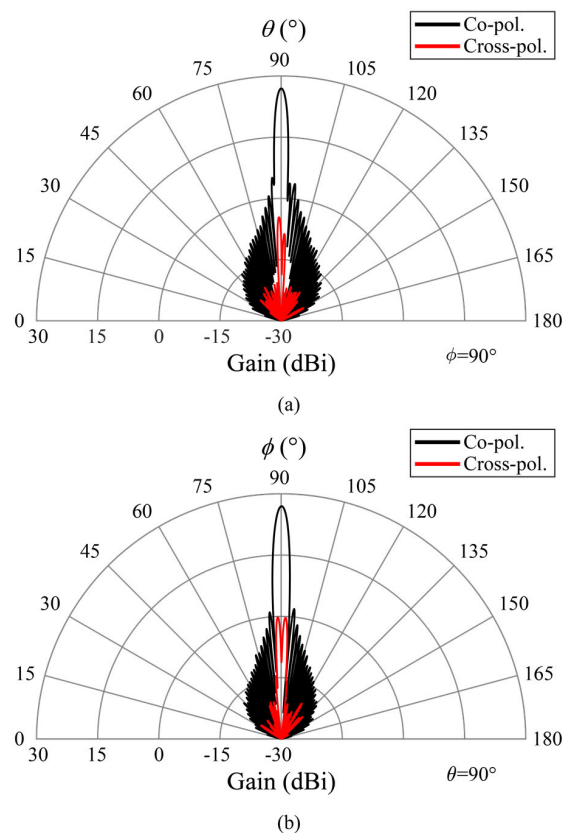
7.0 dBi and a cross-polarization level of 35.0 dB was used as the probe antenna.

The measurement parameters are listed in Table 2. The incident angle was set to 45° and exhibited transverse electric (TE) polarization. The near-field scanning area was chosen to be 191 mm × 191 mm with a 100 mm grid distance consid-

ering the footprint area and evanescent modes. The near field in the scanning area was sampled at a spacing of 3.75 mm ($= \lambda/2$) to prevent aliasing. The maximum observable angle was determined to be $\psi_m = 48.14°$ according to (10). A Keysight E5080B vector network analyzer was configured covering a frequency range of 24-44 GHz with a bandwidth of 20 GHz, ensuring an equivalent pulse width of 50 ps in the time domain. In addition, the frequency sample spacing was chosen to be 20 MHz, which allows for a time window of 50 ns. The unwanted coupling and multipath reflections are eliminated by applying proper gating within the time window.

Fig. 8 shows the plane-wave spectrum obtained by the discrete Fourier transform of the raw data from two different materials. It is reported that the diffuse scattering is normally weak when the standard deviation of surface height satisfies the Rayleigh criterion [14]. However, in this experiment, significant diffuse scattering was observed, as shown in Fig. 8, although the standard deviation of the surface heights for both samples was less than $\lambda/10$. The intensity of diffuse scattering appears to be related not only to the standard deviation of the surface height, but also to statistical parameters such as the correlation length [30].

The reflection coefficient of the MUT can be calculated by substituting the transformed far-field of the PEC and MUT into (12). By integrating the field patterns in the regions of $\theta_r - \psi_m < \theta_s < \theta_r + \psi_m$ and $\phi_r - \psi_m < \phi_s < \phi_r + \psi_m$, reflection coefficients were determined to be 0.773 and 0.648 for the plastered and rolled MUTs, respectively. A directive model pattern was generated with the extracted Γ parameters.

A typically used cost function is the fraction of variance unexplained (FVU) [31]. This potentially ignores the weak diffuse power difference because even a small power difference in the specular direction is dominant. Therefore, we propose the following cost function:

$$C(S, \alpha) = \sum_{\phi_s = \phi_r - \psi_m}^{\phi_r + \psi_m} \sum_{\theta_s = \theta_r - \psi_m}^{\theta_r + \psi_m} \left| f \left(20 \log_{10} \left| \mathbf{E}_{\mathbf{r,MUT}}^{\mathbf{NTFT}}(\theta_s, \phi_s) \right| \right) \right.$$
$$\left. - f \left(20 \log_{10} \left| \mathbf{E}_{\mathbf{r,MUT}}^{\mathbf{model}}(\theta_s, \phi_s) \right| \right) \right|, \quad (16)$$

where f is the envelope function. A logarithmic function was used to emphasize the difference in weak diffuse powers and reduce the difference in the specular direction. However, the logarithmic function overemphasizes the null point differences, especially when the null points of the two field patterns do not match. To avoid dependence on null points, we considered the envelope of the radiation patterns. This envelope was obtained by interpolating the local maximum along θ_s using a cubic spline function for each ϕ_s angle. The local maximum points were determined by taking the maximum point within a sliding window in θ_s, whose width was the 3 dB width of the specular lobe. The range of the summation angle was limited to $\pm\psi_m$ around the specular
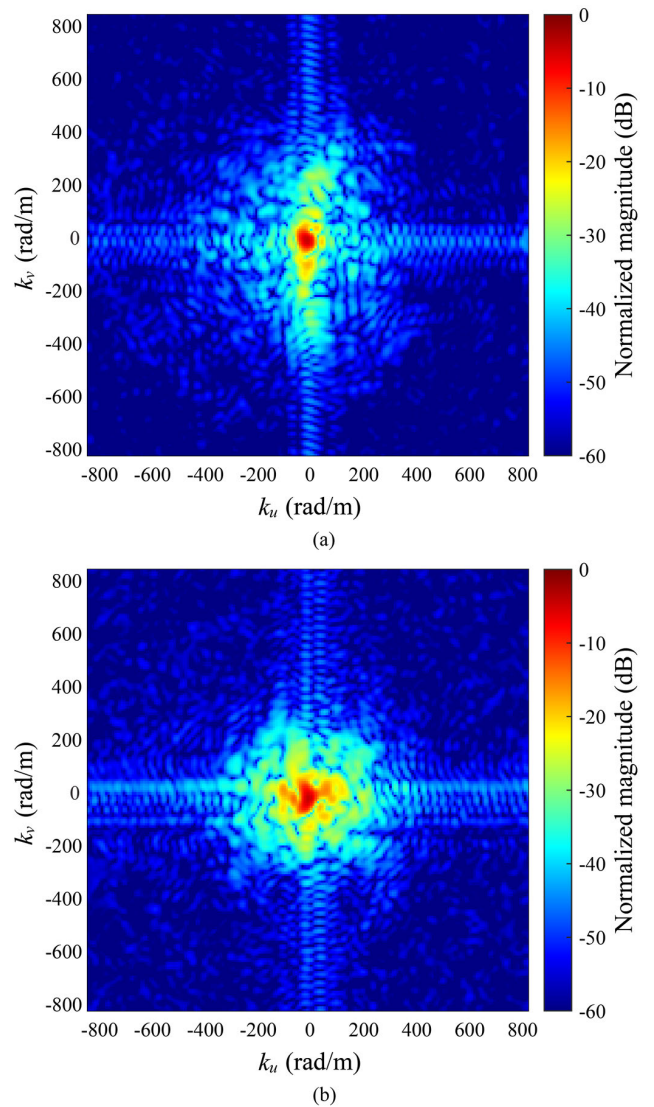

FIGURE 8. Plane-wave spectrum from rough materials formed by (a) plastering and (b) rolling.

direction because a pattern beyond this range is unreliable in PNF scanning.

To validate the proposed method, a conventional free-space measurement method was conducted on the same MUT samples and the FVU was applied. An LB-45500 horn antenna pair was used as the transmitter and receiver, with the transmitter and receiver antennas positioned 3 m and 1 m from the MUT, respectively. Fig. 9 illustrates the values of the cost functions obtained using the conventional and proposed methods. It can be seen that both cost functions are minimized with similar S and α parameters. The minimized values for the plastered MUT were determined to be $|\Gamma| = 0.691$, $|S| = 0.291$, and $\alpha = 113$ for the conventional method, and $|\Gamma| = 0.773$, $|S| = 0.289$, and $\alpha = 65$ for the proposed method. For the rolled MUT, the values were $|\Gamma| = 0.812$,
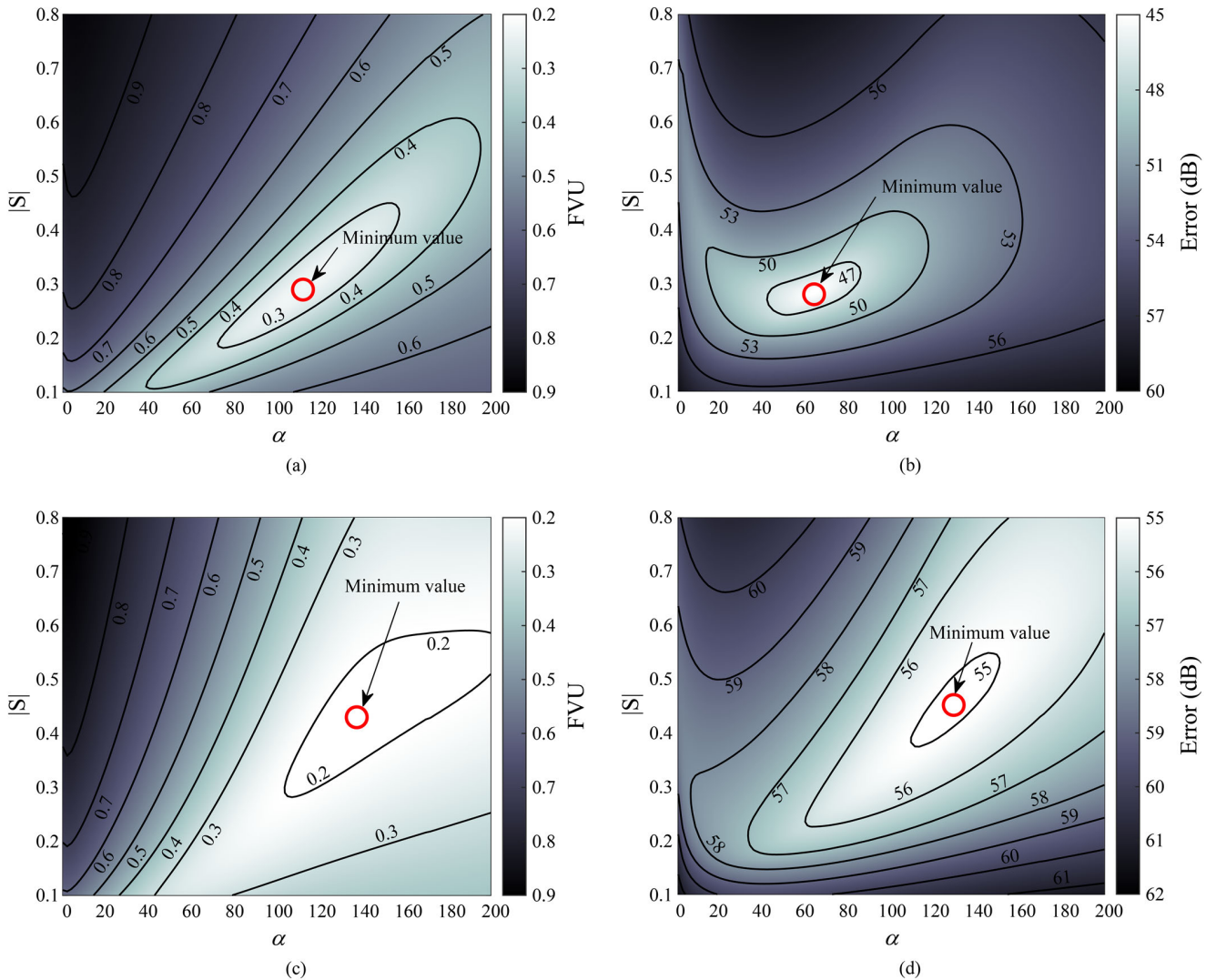
FIGURE 9. Cost function evaluations: (a) plastered MUT with conventional method, (b) plastered MUT with proposed method, (c) rolled MUT with conventional method, and (d) rolled MUT with proposed method.

$|S| = 0.431$, and $\alpha = 137$ for the conventional method, and $|\Gamma| = 0.648$, $|S| = 0.452$, and $\alpha = 129$ for the proposed method. From Fig. 5, the error in the reflection coefficient is estimated to be less than 1% for the smallest value of $\alpha = 65$ with $\psi_m = 48.14°$.

In Fig. 10, the radiation patterns using ER model parameters extracted from 2D near-field measurement data for each cost function are shown and compared with the measurement result. Compared to the results from the proposed cost function, the results from FVU are fitted with higher values of α. In both Fig. 10 (a) and (b), the results from FVU show narrower patterns, which illustrate that the weak diffuse power is underweighted. In Fig. 10(b), the incoherent component from FVU does not increase as high as the measurement pattern near $-10° < \psi < 10°$ due to the coupling between S and R. When a high value of S causes a decrease in R, a significant change in the coherent component around $\psi = 0°$ results

in a large error. The results from the proposed cost function show a similar trend across the range of the summation angle.

The resulting directive model patterns in the plane of incidence for the minimum values of Fig. 9 are compared in Fig. 11. The predicted patterns were similar for both the conventional and proposed methods. The backscattering observed in the measurement near 135° was not modeled in the directive model. If backscattering is necessary, other ER models, such as the double-lobe model, may be considered. Also note that with the plastered MUT, slightly more diffuse scattering was observed near 90° in the proposed method than in the conventional method. As shown in Fig. 8(a), the plane-wave spectrum has an elongated distribution in the vertical direction. The conventional method considers a 1D scan corresponding to the plane-wave spectrum in the plane of incidence ($k_v = 0$). By contrast, the proposed
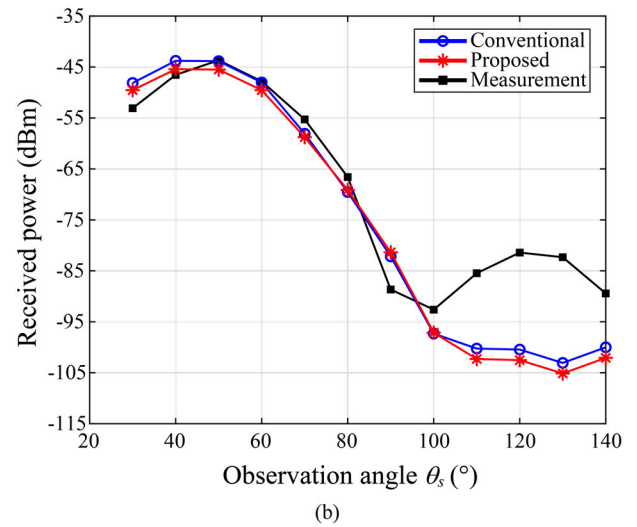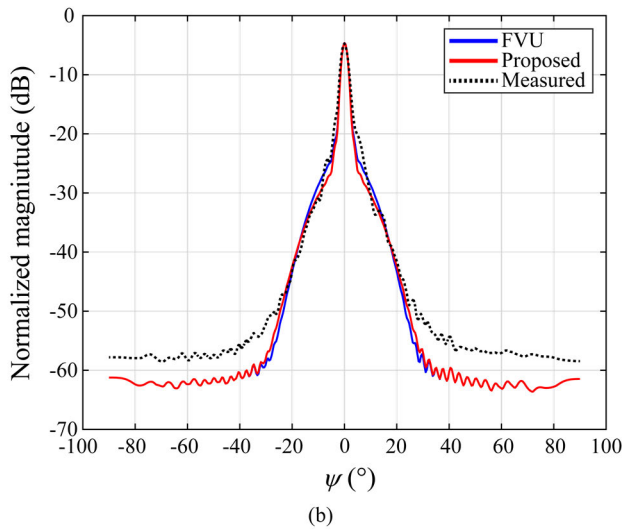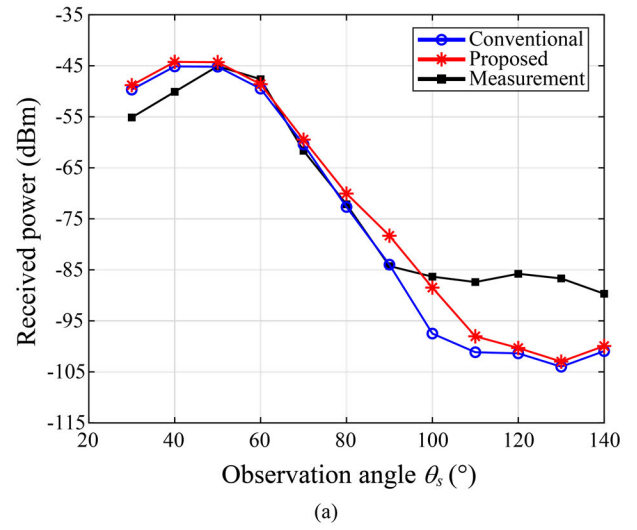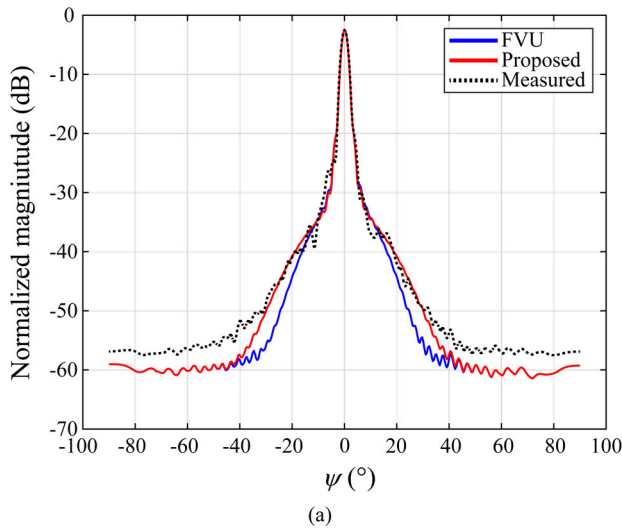
FIGURE 10. Directive model patterns from FVU and proposed cost function on 2D near-field measurement data in comparison with the average of measured pattern for (a) the plastered MUT and (b) rolled MUT.

FIGURE 11. Directive model patterns from conventional and proposed method in comparison with 1D measured pattern for (a) the plastered MUT and (b) rolled MUT.

method considers the entire 2D domain data and produces α parameter that is slightly underestimated in the plane of incidence. Despite these differences in the measurement setup and the algorithms, the pattern in the proposed method followed that of the conventional method, thus confirming the validity of the proposed method.

V. CONCLUSION

In this study, we introduced a compact technique for extracting ER model parameters. This approach involves the generation of a plane wave using a parabolic reflector antenna, the collection of near-field data, the conversion of the near-field data to the far field, and model fitting to the transformed data. Two MUTs exhibiting distinct roughness characteristics were prepared and their diffuse scattering was measured at 40 GHz using both the proposed and conventional methods. Model parameters were extracted using both techniques.

The scattering patterns predicted from these models were compared. This comparison demonstrates that the model derived from our proposed method is consistent with the model obtained using the conventional approach.

The proposed technique incorporates the advantages of a compact range and near-field measurement methods, thereby significantly reducing the size of the measurement setup around the MUT. Consequently, this can serve as an effective method for extracting site-specific model parameters directly from indoor environments for the applications such as the prediction of mm-wave propagation. Although the selected PNF scanning grid exhibited limitations regarding the diffuse scattering angle range, the resulting model proved effective compared with conventional methods. When backscattering also needs to be modeled, spherical near-field scanning coupled with a double-lobe model may be considered.

REFERENCES

[1] K. Abboud, H. A. Omar, and W. Zhuang, "Interworking of DSRC and cellular network technologies for V2X communications: A survey," *IEEE Trans. Veh. Technol.*, vol. 65, no. 12, pp. 9457–9470, Dec. 2016.

[2] G. G. Md. N. Ali, B. Ayalew, A. Vahidi, and M. Noor-A-Rahim, "Analysis of reliabilities under different path loss models in urban/sub-urban vehicular networks," in *Proc. IEEE 90th Veh. Technol. Conf. (VTC-Fall)*, Sep. 2019, pp. 1–6.

[3] J. S. C. Turner, A. B. Shahriman, A. Harun, S. A. Z. Murad, M. N. Isa, R. C. Ismail, D. L. Ndzi, M. S. M. Hashim, Z. M. Razlan, W. K. Wan, and M. F. Ramli, "Modelling on impact of building obstruction for V2I communication link in micro cellular environment," *J. Phys., Conf. Ser.*, vol. 1755, no. 1, Feb. 2021, Art. no. 012031.

[4] M. Shafi, J. Zhang, H. Tataria, A. F. Molisch, S. Sun, T. S. Rappaport, F. Tufvesson, S. Wu, and K. Kitao, "Microwave vs. millimeter-wave propagation channels: Key differences and impact on 5G cellular systems," *IEEE Commun. Mag.*, vol. 56, no. 12, pp. 14–20, Dec. 2018.

[5] M. Lecci, T. Zugno, S. Zampato, and M. Zorzi, "A full-stack open-source framework for antenna and beamforming evaluation in mmWave 5G NR," in *Proc. IEEE Int. Conf. Commun.*, Jun. 2021, pp. 1–6.

[6] S. M. Sabery, A. Bystrov, M. Navarro-Cía, P. Gardner, and M. Gashinova, "Study of low terahertz radar signal backscattering for surface identification," *Sensors*, vol. 21, no. 9, p. 2954, Apr. 2021.

[7] F. Wen and H. Wymeersch, "5G synchronization, positioning, and mapping from diffuse multipath," *IEEE Wireless Commun. Lett.*, vol. 10, no. 1, pp. 43–47, Jan. 2021.

[8] C. Baquero Barneto, E. Rastorgueva-Foi, M. F. Keskin, T. Riihonen, M. Turunen, J. Talvitie, H. Wymeersch, and M. Valkama, "Millimeter-wave mobile sensing and environment mapping: Models, algorithms and validation," *IEEE Trans. Veh. Technol.*, vol. 71, no. 4, pp. 3900–3916, Apr. 2022.

[9] P. Beckmann and A. Spizzichino, *The Scattering of Electromagnetic Waves from Rough Surfaces*. Norwood, MA, USA: Artech House, 1987.

[10] L. Tsang, J. Kong, and K.-H. Ding, *Scattering of Electromagnetic Waves: Theories and Applications*. New York, NY, USA: Wiley, 2000.

[11] L. Tsang, J. Kong, K.-H. Ding, and C. O. Ao, *Scattering of Electromagnetic Waves: Numerical Simulations*. New York, NY, USA: Wiley, 2001.

[12] D. Didascalou, M. Dottling, N. Geng, and W. Wiesbeck, "An approach to include stochastic rough surface scattering into deterministic ray-optical wave propagation modeling," *IEEE Trans. Antennas Propag.*, vol. 51, no. 7, pp. 1508–1515, Jul. 2003.

[13] N. Déchamps, N. de Beaucoudrey, C. Bourlier, and S. Toutain, "Fast numerical method for electromagnetic scattering by rough layered interfaces: Propagation-inside-layer expansion method," *J. Opt. Soc. Amer. A, Opt. Image Sci.*, vol. 23, no. 2, p. 359, Feb. 2006.

[14] N. Pinel and C. Bourlier, "Electromagnetic wave scattering from random rough surfaces: Basics," in *Proc. Electromagnetic Wave Scattering From Random Rough Surfaces: Asymptotic Models*, 1st ed. Hoboken, NJ, USA: Wiley, 2013, pp. 1–39.

[15] V. Degli-Esposti, "A diffuse scattering model for urban propagation prediction," *IEEE Trans. Antennas Propag.*, vol. 49, no. 7, pp. 1111–1113, Jul. 2001.

[16] V. Degli-Esposti, D. Guiducci, A. de'Marsi, P. Azzi, and F. Fuschini, "An advanced field prediction model including diffuse scattering," *IEEE Trans. Antennas Propag.*, vol. 52, no. 7, pp. 1717–1728, Jul. 2004.

[17] V. Degli-Esposti, F. Fuschini, E. M. Vitucci, and G. Falciasecca, "Measurement and modelling of scattering from buildings," *IEEE Trans. Antennas Propag.*, vol. 55, no. 1, pp. 143–153, Jan. 2007.

[18] S. Bakirtzis, T. Hashimoto, and C. D. Sarris, "FDTD-based diffuse scattering and transmission models for ray tracing of millimeter-wave communication systems," *IEEE Trans. Antennas Propag.*, vol. 69, no. 6, pp. 3389–3398, Jun. 2021.

[19] E. M. Vitucci, N. Cenni, F. Fuschini, and V. Degli-Esposti, "A reciprocal heuristic model for diffuse scattering from walls and surfaces," *IEEE Trans. Antennas Propag.*, vol. 71, no. 7, pp. 6072–6083, Jul. 2023.

[20] C. A. Balanis, *Antenna Theory: Analysis and Design*, 4th ed. Hoboken, NJ, USA: Wiley, 2016.

[21] J. Jürveläinen and K. Haneda, "Sixty gigahertz indoor radio wave propagation prediction method based on full scattering model," *Radio Sci.*, vol. 49, no. 4, pp. 293–305, Apr. 2014.

[22] J. Pascual-García, J.-M. Molina-García-Pardo, M.-T. Martínez-Inglés, J.-V. Rodríguez, and N. Saurín-Serrano, "On the importance of diffuse scattering model parameterization in indoor wireless channels at mm-wave frequencies," *IEEE Access*, vol. 4, pp. 688–701, 2016.

[23] F. Sheikh, D. Lessy, M. Alissa, and T. Kaiser, "A comparison study of non-specular diffuse scattering models at terahertz frequencies," in *Proc. 1st Int. Workshop Mobile THz Syst. (IWMTS)*, Jul. 2018, pp. 1–6.

[24] X. Liu and J. Yu, "Effect of quiet zone ripples on antenna pattern measurement," *Prog. Electromagn. Res. M*, vol. 75, pp. 49–60, 2018.

[25] M. H. Francis and R. C. Wittmann, "Near-field scanning measurements: Theory and practice," in *Modern Antenna Handbook*, C. A. Balanis, Ed. Hoboken, NJ, USA: Wiley, 2008, pp. 929–976.

[26] *IEEE Recommended Practice for Near-Field Antenna Measurements*, Standard IEEE Standard 1720, 2012.

[27] E. Joy and D. Paris, "Spatial sampling and filtering in near-field measurements," *IEEE Trans. Antennas Propag.*, vol. AP-20, no. 3, pp. 253–261, May 1972.

[28] M. H. Francis, "Aperture-sampling requirements [and reply]," *IEEE Antennas Propag. Mag.*, vol. 39, no. 5, pp. 76–81, Oct. 1997.

[29] A. C. Newell, "Error analysis techniques for planar near-field measurements," *IEEE Trans. Antennas Propag.*, vol. 36, no. 6, pp. 754–768, Jun. 1988.

[30] M. Alissa, T. Kreul, and T. Kaiser, "The effect of rough surface statistics on diffuse scattering at terahertz frequencies," in *Proc. Eur. Conf. Netw. Commun. (EuCNC)*, Jun. 2019, pp. 118–122.

[31] H. Tian, X. Liao, Y. Wang, Y. Shao, J. Zhou, T. Hu, and J. Zhang, "Effect level based parameterization method for diffuse scattering models at millimeter-wave frequencies," *IEEE Access*, vol. 7, pp. 93286–93293, 2019.
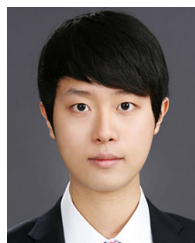
JUNSEOP LEE (Student Member, IEEE) received the B.S. degree in electronics and communication engineering from Hanyang University, Ansan, South Korea, in 2012, and the M.S. degree in mechatronics engineering from the Gwangju Institute of Science and Technology, Gwangju, South Korea, in 2014, where he is currently pursuing the Ph.D. degree.

His current research interests include mixed-signal system design, synthetic-aperture radar, and microwave remote sensing systems.

KANGWOOK KIM (Senior Member, IEEE) received the B.S. degree in electrical engineering from Ajou University, Suwon, South Korea, in 1997, and the M.S. and Ph.D. degrees in electrical and computer engineering from the Georgia Institute of Technology, Atlanta, GA, USA, in 2001 and 2003, respectively.

From 2003 to 2005, he was a Postdoctoral Fellow with the Georgia Institute of Technology, where he was involved in the multimodal landmine-detection system research. From 2005 to 2006, he was with the Samsung Advanced Institute of Technology, Suwon. He joined as a Faculty Member of the Gwangju Institute of Science and Technology, Gwangju, South Korea, in 2006. He focused on the design, analysis, and measurement of pulse-radiating antennas with the Georgia Institute of Technology. His research interests include ground-penetrating radar, ultrawideband antennas, and rapid measurement of electromagnetic fields.

● ● ●